

Transport in multiband systems with hot spots on the Fermi surface: Forward-scattering corrections

Maxim Breitzkreiz,^{1,*} P. M. R. Brydon,² and Carsten Timm^{1,†}

¹*Institute of Theoretical Physics, Technische Universität Dresden, 01062 Dresden, Germany*

²*Condensed Matter Theory Center, Department of Physics,
University of Maryland, College Park, USA 20742*

(Dated: June 6, 2014)

Multiband models with hot spots are of current interest partly because of their relevance for the iron-based superconductors. In these materials, the momentum-dependent scattering off spin fluctuations and the ellipticity of the electron Fermi pockets are responsible for anisotropy of the lifetimes of excitations around the Fermi surface. The deep minima of the lifetimes—the so-called hot spots—have been assumed to contribute little to the transport as is indeed predicted by a simple relaxation-time approach. Calculating forward-scattering corrections to this approximation, we find that the effective transport times are much more isotropic than the lifetimes and that, therefore, the hot spots contribute to the transport even in the case of strong spin-fluctuation scattering. We discuss this effect on the basis of an analytical solution of the Boltzmann equation and calculate numerically the temperature and doping dependence of the resistivity and the Hall, Seebeck, and Nernst coefficients.

PACS numbers: 72.10.Di, 72.15.Lh, 74.70.Xa, 74.25.F-

I. INTRODUCTION

Many materials of high current interest for condensed matter physics are metals with strong spin fluctuations, for example doped cuprates and iron pnictides. In both classes, spin fluctuations are thought to mediate the superconducting pairing at relatively high temperatures.^{1,2} Spin fluctuations are also crucial in the normal state, where they provide an important scattering mechanism and thus strongly affect transport. The transport properties of the pnictides are nevertheless quite distinct from the cuprates and show unusual temperature dependences.^{3–11} The main ingredients needed for the description of transport in these systems have been controversially discussed.^{12–15}

The scattering of electrons off spin fluctuations is governed by the spin susceptibility. Close to an antiferromagnetic instability, the susceptibility is strongly peaked in momentum space in the vicinity of the possible ordering vectors \mathbf{Q} . Transport in such systems can thus often be understood based on the concept of hot and cold regions of the Fermi surfaces.^{16,17} The hot regions are the parts of the Fermi surfaces that are connected by the possible ordering vectors \mathbf{Q} . The scattering is particularly strong in these regions. Conversely, in the cold regions not connected by ordering vectors the scattering rate is lower. If the difference in the scattering rate is large, i.e., close to the instability, transport is thus dominated by the cold regions with high conductivity, and the hot regions are then said to be “short-circuited.”

The concept of hot and cold regions generally explains the experimental observations for cuprates and was implicitly assumed to hold also for the pnictides.^{8,10–12} An analysis of the lifetimes of excited electrons close to the Fermi surfaces seems to support this picture,¹³ with the imperfect nesting of electron and hole Fermi pockets nat-

urally leading to the appearance of hot and cold regions with short and long lifetimes, respectively.

Within the *relaxation-time approximation* (RTA), in which the complex relaxation dynamics of each state is modeled by a simple exponential decay, the transport relaxation time is approximated by the lifetime. Since the conductivity is directly proportional to the relaxation time, the states with short lifetimes then do not contribute significantly to the transport. In this paper we show that in multiband systems this effect can be compensated if the forward-scattering corrections to the RTA are taken into account.

Forward-scattering corrections, which are equivalent to vertex corrections in the Kubo formalism, have been studied extensively for one-band models relevant for cuprates and heavy-fermion systems.¹⁸ The pnictides are, in contrast, multiband systems with electron and hole Fermi pockets. The study of two-band models with circular Fermi pockets has shown that forward-scattering corrections to the RTA are huge close to the antiferromagnetic instability and that they give rise to transport anomalies such as a large enhancement of the Hall coefficient^{14,15} and negative magnetoresistance.¹⁵ The minority carriers, i.e., the carriers on the smaller Fermi pocket, were found to exhibit negative transport times, indicating a drift in the direction opposite of what one would expect based on their charge. However, in the simplified models with circular Fermi pockets all states on a given Fermi pocket are equivalent because of rotational symmetry. They are thus unable to address the concept of hot and cold regions, which only appear for noncircular Fermi pockets.

In this article we present a semiclassical Boltzmann theory of transport for a two-band model with elliptical electron pockets relevant for the iron pnictides. We show that due to the forward scattering, the hot-spot picture

fails for the pnictides even for very strong spin fluctuations and highly elliptical electron pockets. In contrast to the lifetimes, which are highly anisotropic around the Fermi pockets with deep minima at the hot spots, the effective transport relaxation times are found to be much more isotropic and to show no special features at the hot spots. Our approximate analytical solution of the Boltzmann equation provides insight into the mechanism behind this effect: The anisotropy of the spin-fluctuation scattering extends the effective relaxation time. At the hot spots, the reduction of the relaxation time due to the stronger scattering is thus compensated by the extension due to the higher anisotropy.

To elucidate the consequences of this mechanism, we calculate numerically the temperature-dependent transport coefficients from the full Boltzmann equation and compare them to the analytical solution and the RTA, finding that the RTA makes qualitatively incorrect predictions. For strongly momentum-dependent scattering, we find large transport anomalies as well as a strong doping dependence.

The remainder of this paper is organized as follows: In Secs. II and III, we present the two-band model, give expressions for the scattering rates, and set up the Boltzmann equation for our model. To gain insight into the physics, we present in Sec. IV an analytical solution to leading order in the ellipticities of the electron pockets. Higher-order corrections are discussed in the appendix. In Sec. V, we present full numerical solutions of the Boltzmann equations. We also calculate the temperature dependence of the resistivity and the Hall, Seebeck, and Nernst coefficients. Finally, we draw some conclusions in Sec. VI.

II. MODEL

We model the FeAs layers of the iron pnictides by an effective two-dimensional two-band model with the dispersions in the single-iron unit cell¹ given by¹⁹

$$\varepsilon_{h\mathbf{k}} = \varepsilon_h - \mu + 2t_h (\cos k_x a + \cos k_y a), \quad (1)$$

$$\varepsilon_{e\mathbf{k}} = \varepsilon_e - \mu + t_{e,1} \cos k_x a \cos k_y a - t_{e,2} \xi (\cos k_x a + \cos k_y a), \quad (2)$$

where a is the iron-iron separation. As illustrated in Fig. 1, the band h gives rise to a nearly circular hole Fermi pocket at the center of the Brillouin zone, while the band e forms two electron pockets $e1$ and $e2$, displaced by $\mathbf{Q}_{e1} = (0, \pi/a)$ and $\mathbf{Q}_{e2} = (\pi/a, 0)$, respectively. The parameter ξ controls the ellipticity of the electron pockets. The chemical potential μ is determined by the filling n , i.e., the number of electrons per unit cell, which can be tuned by doping in the pnictides. The filling n determines the sizes of the Fermi pockets. For $n \approx 2.08$ the areas of the three pockets are nearly equal, while for smaller (larger) n the hole pocket (electron pockets) become larger. Following Ref. 19, we take $\varepsilon_h = -3.5t_h$, $\varepsilon_e = 3t_h$, $t_{e,1} = 4t_h$ and $t_{e,2} = t_h$.

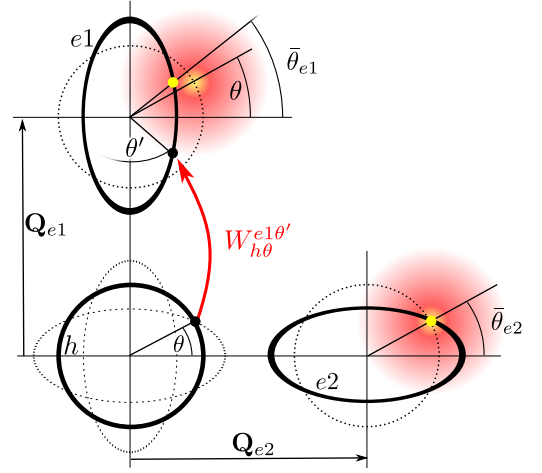


Figure 1. (Color online) Illustration of the Fermi pockets and the scattering rates. An electron in state $|h, \theta\rangle$ is scattered to $|e1, \theta'\rangle$. The yellow (light gray) dots indicate the maxima of the scattering rates $W_{h\theta}^{e1\theta'}$ and $W_{h\theta}^{e2\theta'}$ as functions of the polar angle θ' on the target Fermi pocket. The maxima stem from the enhanced spin susceptibility (color gradient) for the scattering wave vectors \mathbf{Q}_{e1} and \mathbf{Q}_{e2} . The thin dotted lines show the Fermi surfaces displaced by the nesting vectors. The hot spots are located at the resulting crossing points.

It is widely accepted that repulsive interactions between the nested electron and hole pockets drive a magnetic instability towards a stripe spin-density wave in the pnictide parent compounds with magnetic ordering vector \mathbf{Q}_{e1} or \mathbf{Q}_{e2} .²⁰ Above the magnetic transition temperature, we therefore expect that the spin susceptibility will display pronounced peaks at these vectors. Because of the ellipticity of the electron pockets, however, the nesting is imperfect and distinct hot spots develop at the points on the electron and hole Fermi pockets separated by \mathbf{Q}_{e1} or \mathbf{Q}_{e2} , see Fig. 1. The positions of the hot spots change with the doping:^{12,19} for underdoping ($n < 2.08$) the hot spots are located near the major axis of the electron pockets, while at overdoping ($n > 2.08$) the hot spots shift to the minor axis. On the hole pocket, the hot spots shift from the axes to the diagonal and back again as one dopes across the antiferromagnetic dome.

We assume that the transport behavior is dominated by the scattering off spin fluctuations, which we model by the phenomenological susceptibility proposed by Millis, Monien, and Pines,²¹ with temperature-dependent parameters based on neutron-scattering experiments.²² Although this ignores the anisotropy of the magnetic excitations in the pnictides caused by the ellipticity of the electron Fermi pockets,²³ we shall see that the precise form of the susceptibility is less important for the transport than the anisotropy of the scattering rate. Together with momentum-independent impurity scattering, the scattering rate from a single-electron state $|b, \mathbf{k}\rangle$ to a state $|b', \mathbf{k}'\rangle$, where $b = e, h$ denotes the band, can be

written as²⁴

$$W_{b\mathbf{k}}^{b'\mathbf{k}'} = (1 - \delta_{bb'}) W_{\text{sf}} \frac{p_T(\varepsilon_{b\mathbf{k}} - \varepsilon_{b'\mathbf{k}'})}{(\varepsilon_{b\mathbf{k}} - \varepsilon_{b'\mathbf{k}'})^2 + \omega_{\mathbf{k},\mathbf{k}'}^2} + \delta(\varepsilon_{b\mathbf{k}} - \varepsilon_{b'\mathbf{k}'}) W_{\text{imp}}, \quad (3)$$

where W_{sf} and W_{imp} represent the overall strength of the scattering off spin fluctuations and impurities, respectively, $p_T(x) \equiv x (\coth x/2k_B T - \tanh x/2k_B T)$, and

$$\omega_{\mathbf{k},\mathbf{k}'} \equiv \Gamma_T \left(1 + \xi_T^2 \min_{\mathbf{Q}} [(\mathbf{k} - \mathbf{k}' + \mathbf{Q})^2] \right), \quad (4)$$

where the four possible values for \mathbf{Q} are $\pm \mathbf{Q}_{e1}$ and $\pm \mathbf{Q}_{e2}$. With the Curie-Weiss temperature $-\theta_{\text{CW}} < 0$, the frequency scale and the correlation length are given by^{14,22} $\Gamma_T = \Gamma_0 (T + \theta_{\text{CW}})/\theta_{\text{CW}}$ and $\xi_T = \xi_0 \sqrt{\theta_{\text{CW}}/(T + \theta_{\text{CW}})} \exp(-T/T_0)$, respectively. Following Ref. 14, we here introduce an additional exponential decay of ξ_T to account for the high-temperature behavior and choose $T_0 = 200$ K. Following Ref. 22, we take $\xi_0 = 10a$, $\theta_{\text{CW}} = 30$ K and $\Gamma_0 = 4.2$ meV. The resulting form of $\omega_{\mathbf{k},\mathbf{k}'}$ and thus $W_{b\mathbf{k}}^{b'\mathbf{k}'}$ is only valid as long as the system does not order antiferromagnetically or becomes superconducting.

The transport is governed by states on the Fermi pockets, denoted by $|s, \theta\rangle$, where $s = h, e1, e2$ is the pocket index and θ is the polar angle along the pocket, see Fig. 1. From Eq. (3) we see that in the low-temperature regime, $k_B T \ll \varepsilon_F$, the scattering rate is sharply peaked at $\varepsilon_{b\mathbf{k}} = \varepsilon_{b'\mathbf{k}'}$ so that scattering is nearly elastic. We exploit this fact by writing

$$W_{b\mathbf{k}_F}^{b'\mathbf{k}'} \approx \delta(\varepsilon_{b'\mathbf{k}'} - \varepsilon_F) W_{s\theta}^{s'\theta'}, \quad (5)$$

where

$$W_{s\theta}^{s'\theta'} \equiv (1 - \delta_{ss'}) W_{\text{sf}} \int d\varepsilon \frac{p_T(\varepsilon)}{\varepsilon^2 + \omega_{\mathbf{k},\mathbf{k}'}^2} + W_{\text{imp}} \quad (6)$$

is the effective elastic scattering rate between states on the Fermi pockets s, s' belonging to the bands b, b' . Since the spin susceptibility and thus $W_{b\mathbf{k}}^{b'\mathbf{k}'}$ is strongly momentum dependent, the elastic scattering rate $W_{s\theta}^{s'\theta'}$ strongly depends on the angles θ and θ' , in particular on the change in angle, $\theta' - \theta$. This is what we call *anisotropic* scattering in the following.

More specifically, the scattering anisotropy stems from the peaks in the spin susceptibility at the wave vectors $\pm \mathbf{Q}_{e1}$ and $\pm \mathbf{Q}_{e2}$. For an initial state $|h, \theta\rangle$ with wave vector \mathbf{k} , the scattering rate has maxima for the final states $|e1, \bar{\theta}_{e1}\rangle$ and $|e2, \bar{\theta}_{e2}\rangle$, defined as the states on the Fermi pockets $e1, e2$ with wave vectors closest to $\mathbf{k} + \mathbf{Q}_{e1}$ and $\mathbf{k} + \mathbf{Q}_{e2}$, respectively, see Fig. 1. Similarly, for an initial state $|e1, \theta\rangle$ ($|e2, \theta\rangle$) with wave vector \mathbf{k} , the scattering rate has a maximum for the final state $|h, \bar{\theta}_h\rangle$ with wave vector closest to $\mathbf{k} - \mathbf{Q}_{e1}$ ($\mathbf{k} - \mathbf{Q}_{e2}$), where $\bar{\theta}_h \approx \theta$ since the hole pocket is nearly circular.

The scattering rate summed over all final states determines the characteristic lifetime of the state $|s, \theta\rangle$,

$$\tau_{s\theta} = \left(\frac{1}{2\pi} \sum_{s'} \int d\theta' N_{s'\theta'} W_{s\theta}^{s'\theta'} \right)^{-1}, \quad (7)$$

where $N_{s\theta} = |d\mathbf{k}_{F,s\theta}/d\theta|/\pi\hbar|\mathbf{v}_{F,s\theta}|$ is the density of states, with the spin degeneracy included, of pocket s at the polar angle θ and $\mathbf{k}_{F,s\theta}$ and $\mathbf{v}_{F,s\theta}$ are the Fermi momentum and the Fermi velocity, respectively. In contrast to the transport relaxation time, which will be discussed below, the lifetime only depends on the integrated scattering strength and is independent of the precise shape of $W_{s\theta}^{s'\theta'}$ as a function of θ' .

III. BOLTZMANN FORMALISM

Our starting point is the semiclassical Boltzmann transport equation for a multiband system,

$$-f'_0(\varepsilon_{b\mathbf{k}}) \mathbf{E} \cdot \mathbf{v}_{b\mathbf{k}} - \frac{e}{\hbar} \mathbf{B} \cdot (\mathbf{v}_{b\mathbf{k}} \times \nabla_{\mathbf{k}}) g_{b\mathbf{k}} = \sum_{b'\mathbf{k}'} W_{b\mathbf{k}}^{b'\mathbf{k}'} (g_{b\mathbf{k}} - g_{b'\mathbf{k}'}), \quad (8)$$

where $\mathbf{E} = (E_x, E_y, 0)$ and $\mathbf{B} = (0, 0, B)$ are weak uniform electric and magnetic fields, respectively, $\mathbf{v}_{b\mathbf{k}} \equiv \hbar^{-1} \nabla_{\mathbf{k}} \varepsilon_{b\mathbf{k}}$ is the velocity and $g_{b\mathbf{k}} \equiv f_{b\mathbf{k}} - f_0(\varepsilon_{b\mathbf{k}})$ is the difference between the non-equilibrium distribution function $f_{b\mathbf{k}}$ and the Fermi-Dirac distribution $f_0(\varepsilon_{b\mathbf{k}})$. This difference is of the general form^{25–27}

$$g_{b\mathbf{k}} = -f'_0(\varepsilon_{b\mathbf{k}}) \mathbf{E} \cdot (\mathbf{\Lambda}_{b\mathbf{k}} + \delta \mathbf{\Lambda}_{b\mathbf{k}}), \quad (9)$$

with the as yet unknown vector mean free path $\mathbf{\Lambda}_{b\mathbf{k}} + \delta \mathbf{\Lambda}_{b\mathbf{k}}$. Here, $\mathbf{\Lambda}_{b\mathbf{k}}$ ($\delta \mathbf{\Lambda}_{b\mathbf{k}}$) is of zero (first) order in the magnetic field \mathbf{B} . For states on the Fermi pockets we write $\mathbf{\Lambda}_{s\theta}$, $\delta \mathbf{\Lambda}_{s\theta}$ with obvious definitions.

Inserting Eqs. (5), (6), and (9) into the Boltzmann equation (8) and using $\sum_{b'\mathbf{k}'} = \sum_{s'} \int \frac{d\theta'}{2\pi} N_{s'\theta'} \int d\varepsilon_{b'\mathbf{k}'}$, one finds for states at the Fermi energy²⁷

$$\mathbf{\Lambda}_{s\theta} = \tau_{s\theta} \mathbf{v}_{s\theta} + \tau_{s\theta} \sum_{s'} \int \frac{d\theta'}{2\pi} N_{s'\theta'} W_{s\theta}^{s'\theta'} \mathbf{\Lambda}_{s'\theta'}, \quad (10)$$

$$\delta \mathbf{\Lambda}_{s\theta} = \tau_{s\theta} \eta_s \frac{eB}{\pi\hbar^2} \frac{1}{N_{s\theta}} \frac{\partial \mathbf{\Lambda}_{s\theta}}{\partial \theta} + \tau_{s\theta} \sum_{s'} \int \frac{d\theta'}{2\pi} N_{s'\theta'} W_{s\theta}^{s'\theta'} \delta \mathbf{\Lambda}_{s'\theta'}, \quad (11)$$

where $\eta_h = 1$ and $\eta_{e1} = \eta_{e2} = -1$. The RTA consists of neglecting the forward-scattering corrections in Eqs. (10) and (11), i.e., the second terms on the right-hand sides. Thus in the RTA one obtains

$$\mathbf{\Lambda}_{s\theta} = \mathbf{\Lambda}_{s\theta}^{(0)} \equiv \tau_{s\theta} \mathbf{v}_{s\theta}, \quad (12)$$

$$\delta \mathbf{\Lambda}_{s\theta} = \delta \mathbf{\Lambda}_{s\theta}^{(0)} \equiv \tau_{s\theta} \eta_s \frac{eB}{\pi\hbar^2} \frac{1}{N_{s\theta}} \frac{\partial \mathbf{\Lambda}_{s\theta}^{(0)}}{\partial \theta}. \quad (13)$$

Evidently, within the RTA the solution is determined by the bare lifetimes $\tau_{s\theta}$ given in Eq. (7). The RTA becomes exact if the scattering rate is isotropic around the Fermi pockets so that the forward-scattering corrections average out. For a nonzero scattering anisotropy, however, the result may differ significantly from the RTA.¹⁵

The charge current $\mathbf{J} = \sigma \mathbf{E}$ is controlled by the conductivity tensor σ , which is in turn determined by the vector mean free path,²⁷

$$\sigma^{ij} = e^2 \sum_s \int \frac{d\theta}{2\pi} N_{s\theta} v_{s\theta}^i (\Lambda_{s\theta}^j + \delta \Lambda_{s\theta}^j) \equiv \sum_s \int \frac{d\theta}{2\pi} \sigma_{s\theta}^{ij}. \quad (14)$$

Writing $\mathbf{E} = E (\cos \phi, \sin \phi, 0)$, we find the current parallel to the electric field as

$$\begin{aligned} \frac{\mathbf{J} \cdot \mathbf{E}}{E} &= \sum_s \int \frac{d\theta}{2\pi} (\sigma_{s\theta}^{xx} \cos^2 \phi + \sigma_{s\theta}^{yy} \sin^2 \phi \\ &\quad + \sigma_{s\theta}^{xy} \cos \phi \sin \phi + \sigma_{s\theta}^{yx} \cos \phi \sin \phi) \\ &\equiv \sum_s \int \frac{d\theta}{2\pi} J_{s\theta}, \end{aligned} \quad (15)$$

where $J_{s\theta}$ is the contribution of the state $|s, \theta\rangle$ to the current.

IV. ANALYTICAL RESULTS

To gain insight into transport beyond the RTA, we now construct an approximate analytical solution of Eqs. (10) and (11) that fully accounts for the anisotropic scattering. We will first discuss a few reasonable assumptions that make an analytical solution feasible. The full numerical solution is discussed in Sec. V.

As illustrated in Fig. 1, the scattering rate $W_{s\theta}^{s'\theta'}$ understood as a function of θ' has a maximum at $\theta' = \bar{\theta}_{s'}$, which of course depends on θ . The small difference between θ and $\bar{\theta}_{s'}$ stems from the ellipticity of the electron pockets. We now make two simplifying assumptions: (i) The peak of the scattering rate $W_{s\theta}^{s'\theta'}$ as a function of θ' is assumed to be symmetric around $\theta' = \bar{\theta}_{s'}$, and (ii) the peak width is small on the scale on which the Fermi velocity $|\mathbf{v}_{s\theta}|$ and the density of states $N_{s\theta}$ vary. Both assumptions become exact in the limit of very strongly peaked spin susceptibility, i.e., as the magnetic instability is approached. In the opposite limit of isotropic scattering, the forward-scattering corrections cancel out so that we also obtain the exact results.

On the right-hand side of Eq. (10), we split $\Lambda_{s'\theta'}$ into contributions parallel and perpendicular to $\Lambda_{s'\bar{\theta}_{s'}}$,

$$\Lambda_{s'\theta'} = \frac{|\Lambda_{s'\theta'}|}{|\Lambda_{s'\bar{\theta}_{s'}}|} [\Lambda_{s'\bar{\theta}_{s'}} \cos(\theta' - \bar{\theta}_{s'}) + \hat{\mathbf{z}} \times \Lambda_{s'\bar{\theta}_{s'}} \sin(\theta' - \bar{\theta}_{s'})]. \quad (16)$$

By virtue of the assumptions (i) and (ii), the sine term drops out and we obtain

$$\Lambda_{s\theta} = \Lambda_{s\theta}^{(0)} + \left(1 - \frac{1}{2} \delta_{s,h}\right) \sum_{s'} a_{s\theta}^{s'} \Lambda_{s'\bar{\theta}_{s'}}, \quad (17)$$

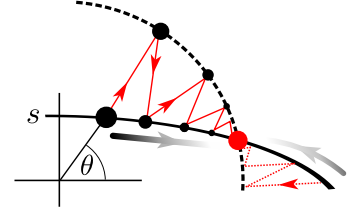


Figure 2. (Color online) Sketch of multiple scattering. During the process, an electron initially in state $|s, \theta\rangle$ effectively scatters between Fermi pockets towards the closest hot spot (red/gray dot). The sequence of states (black dots) is given by the maximum of the scattering rate. Their decreasing contribution to the vector mean free path Λ of the original state $|s, \theta\rangle$ is indicated by the decreasing size of the dots.

where

$$a_{s\theta}^{s'} \equiv (1 + \delta_{s,h}) \tau_{s\theta} \int \frac{d\theta'}{2\pi} N_{s'\theta'} W_{s\theta}^{s'\theta'} \cos(\theta' - \bar{\theta}_{s'}) \quad (18)$$

parametrizes the scattering anisotropy and in the following will be referred to as the *anisotropy parameter*. The Kronecker symbols $\delta_{s,h}$ appearing in Eqs. (17) and (18) ensure that $a_{s\theta}^{s'} \in [0, 1]$ and that $a_{s\theta}^{s'} \rightarrow 1$ corresponds to the limit of strong scattering anisotropy, $W_{s\theta}^{s'\theta'} \propto \delta(\theta' - \bar{\theta}_{s'})$, while $a_{s\theta}^{s'} \rightarrow 0$ gives the case of isotropic scattering, where the RTA result is recovered.

Iterating Eq. (17), we obtain Λ in terms of $\Lambda^{(0)}$ as a power series in the anisotropy parameter. We now discuss the states appearing in this series. The zero-order contribution to $\Lambda_{s\theta}$ is of course $\Lambda_{s\theta}^{(0)}$, the RTA result for the same state $|s, \theta\rangle$. The first-order term involves $\Lambda_{s'\bar{\theta}_{s'}}^{(0)}$ for the state $|s', \bar{\theta}_{s'}\rangle$. This is the *final* state on the Fermi pocket $s' \neq s$ to which the *initial* state $|s, \theta\rangle$ has the largest scattering rate. Due to the ellipticity of the electron pockets, the shift of the angle, $\bar{\theta}_{s'} - \theta$, is always directed towards the closest hot spot, i.e., the intersection of the Fermi pocket s with pocket s' shifted by the appropriate vector \mathbf{Q} . The state appearing in the second-order term is the one reached from $|s', \bar{\theta}_{s'}\rangle$ with the largest scattering rate, again shifted towards the closest hot spot. The states appearing in all higher-order terms are obtained in the same way. The whole process can be interpreted as an effective hopping of the electron along a sequence of states, as illustrated by Fig. 2.

The contribution to $\Lambda_{s\theta}$ from $\Lambda_{s_\nu \theta_\nu}^{(0)}$ of the state $|s_\nu, \theta_\nu\rangle$ reached after ν hopping events involves the product of ν anisotropy parameters at $\theta, \theta_1, \dots, \theta_{\nu-1}$. Since the angular shift between successive hopping events is due to the ellipticity of the electron pockets, and vanishes for a purely circular pocket, it is small for small ellipticities. Indeed, in the appendix we show that for a circular hole pocket and a single elliptical electron pocket the error in the vector mean free path is of *fourth* order in the eccentricity of the electron pocket. If we henceforth neglect this shift, i.e., let $\theta_\nu \approx \theta_{\nu-1}$ for all ν , we incur an error that is small for the moderate ellipticities of the

electron Fermi pockets of the pnictides. In the following section we shall see that this convenient approximation generally compares well with the full numerical solution of Eqs. (10) and (11).

Accordingly setting $\bar{\theta}_{s'} = \theta$ in Eq. (17), the vector mean free paths for different θ decouple and we obtain

$$\Lambda_{h\theta} = \frac{\Lambda_{h\theta}^{(0)} + \frac{1}{2} (a_{h\theta}^{e1} \Lambda_{e1\theta}^{(0)} + a_{h\theta}^{e2} \Lambda_{e2\theta}^{(0)})}{1 - \frac{1}{2} (a_{h\theta}^{e1} a_{e1\theta}^h + a_{h\theta}^{e2} a_{e2\theta}^h)}, \quad (19)$$

$$\Lambda_{e1\theta} = \Lambda_{e1\theta}^{(0)} + a_{e1\theta}^h \Lambda_{h\theta}, \quad (20)$$

$$\Lambda_{e2\theta} = \Lambda_{e2\theta}^{(0)} + a_{e2\theta}^h \Lambda_{h\theta}. \quad (21)$$

Results for the magnetic part $\delta\Lambda_{s\theta}$ can be found analogously by replacing Λ by $\delta\Lambda$ and $\Lambda^{(0)}$ by

$$\tau_{s\theta} \eta_s \frac{eB}{\pi \hbar^2} \frac{1}{N_{s\theta}} \frac{\partial \Lambda_{s\theta}}{\partial \theta}, \quad (22)$$

cf. Eq. (11). Since the anisotropy parameters $a_{s\theta}^{s'}$ are the only parameters in the solution, apart from the RTA vector mean free paths, we will refer to these expressions as the *anisotropy approximation* (AA). Clearly, for $a_{s\theta}^{s'} \neq 0$ the vector mean free paths involve the RTA solutions of all three Fermi pockets. This coupling between the pockets becomes stronger for larger anisotropy parameters. Additionally, the denominator in Eq. (19), which appears in all results, provides a factor that is larger than unity. In the anisotropic limit, $a_{s\theta}^{s'} \rightarrow 1$, the vector mean free paths $\Lambda_{s\theta}$ of all three pockets at a certain angle θ become equal and diverge. Thus, for strong scattering anisotropy the vector mean free path of the minority carriers must be *inverted* relative to the RTA result $\Lambda_{s\theta}^{(0)} \propto \mathbf{v}_{s\theta}$.

Semiclassically, we can interpret our results as follows. The solution to the Boltzmann equation describes a non-equilibrium stationary state in which the acceleration of the electrons due to external forces is balanced by scattering. The vector mean free path of state $|s, \theta\rangle$ can be understood as the displacement that an electron suffers until its velocity $\mathbf{v}_{s\theta}$ is randomized by scattering. The lifetime $\tau_{s\theta}$ is the mean time between two scattering events. If the scattering is isotropic the velocity is randomized after a single scattering event and the vector mean free path thus reads $\tau_{s\theta} \mathbf{v}_{s\theta} \equiv \Lambda_{s\theta}^{(0)}$. On the other hand, anisotropic scattering only partially randomizes the velocity so that the effective relaxation time exceeds the lifetime $\tau_{s\theta}$, giving rise to multiple scattering during the relaxation, see Fig. 2. The enhancement by denominator in Eq. (19) accounts for this fact. In the extreme limit of $a_{s\theta}^{s'} \rightarrow 1$, the factor diverges, indicating that the velocities cannot relax at all and the vector mean free paths become infinite.

This physical picture also applies to the case of two *circular* Fermi pockets considered in Refs. 14 and 15. Because of rotational symmetry, the vector mean free path is parallel to the velocity in that case, and the AA becomes exact. This permits a simple description in terms of transport times. However, we are here concerned with *noncircular* Fermi pockets, which means that the vector

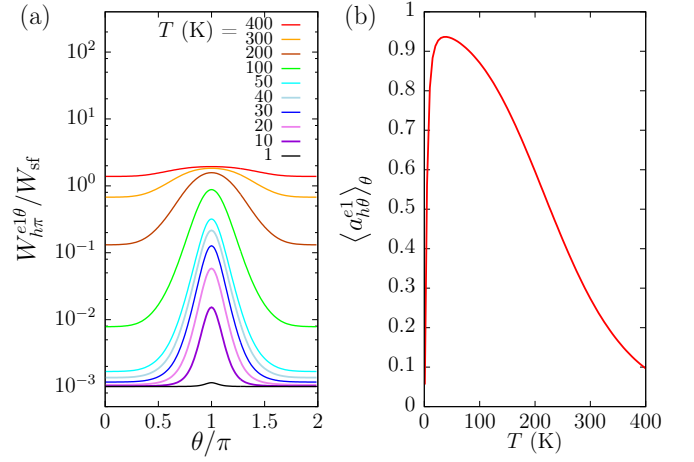


Figure 3. (Color online) (a) Scattering rate at different temperatures for an electron in state $|h, \pi\rangle$ on the hole pocket to scatter to the state $|e1, \theta\rangle$ on the electron pocket $e1$, as a function of the final-state angle θ . (b) Temperature dependence of the anisotropy parameter averaged over all angles θ for the scattering shown in panel (a). The parameters have been set to $\xi = 1$, $n = 2.08$, and $W_{\text{imp}}/W_{\text{sf}} = 10^{-3}$.

mean free path is generally not parallel to the velocity. The common feature is that strong anisotropic scattering forces the vector mean free path of electron and hole pockets at θ to point in the same direction, which is set by the majority carriers. In the relevant parameter range for our model, we will find that the direction is set by the electrons since there are two electron pockets. A change of the dominant carrier type can only be achieved by strong hole doping.

V. NUMERICAL RESULTS

To obtain quantitative results without further approximations beyond the choice of the model and the semiclassical transport theory, we calculate the scattering rate given in Eq. (6) by numerical integration. Furthermore, we discretize the polar angle θ , choosing 160 sites on each Fermi pocket. We have checked that taking more points does not significantly change the results. The lifetimes, Eq. (7), and the anisotropy parameters, Eq. (18), are obtained by summation over the discrete sites. Finally, Eqs. (10) and (11) are solved numerically by matrix inversion. The numerical results will be compared to the AA, which is given by inserting the lifetimes and the anisotropy parameters into Eqs. (19)–(21).

A. Scattering rate

Figure 3(a) shows the temperature dependence of the scattering rate for $\xi = 1$ in Eq. (2) and $W_{\text{imp}}/W_{\text{sf}} = 10^{-3}$. While at high temperatures the scattering rate

is isotropic, at lower temperatures a peak due to spin fluctuations develops corresponding to scattering vectors close to \mathbf{Q}_{e1} or \mathbf{Q}_{e2} . The peak becomes sharper as the temperature is lowered so that the scattering anisotropy increases. At very low temperatures spin fluctuations freeze out and only the isotropic impurity scattering remains so that the anisotropy vanishes again. In Fig. 3(b) we plot the anisotropy parameter corresponding to the scattering rate shown in Fig. 3(a), averaged over the Fermi pocket. It clearly exhibits the increase for decreasing temperature and the final sharp downturn at very low temperatures. Note that in real pnictides, this low-temperature behavior will in most cases be preempted by antiferromagnetic or superconducting order, which are not described by our model spin susceptibility.

B. Hot-spot picture

In this subsection we explore how different parts of the Fermi pockets contribute to the transport. In particular, we want to find out to what extent the concept of hot and cold regions is applicable. Choosing $T = 1$ K and $W_{\text{imp}}/W_{\text{sf}} = 0$, we focus on the regime of strong spin fluctuations with strong scattering anisotropy, where the difference between the RTA and the full result is the most striking.

The current parallel to the electric field is given by Eq. (15). The state-resolved current contributions $J_{s\theta}$ depend on the direction of the electric field due to the noncircular Fermi pockets but we are here not interested in this dependence and therefore average $J_{s\theta}$ over all directions of the electric field in the xy -plane. For $\mathbf{B} = 0$ this gives

$$J_{s\theta} \equiv e^2 N_{s\theta} \frac{v_{s\theta}^x \Lambda_{s\theta}^x + v_{s\theta}^y \Lambda_{s\theta}^y}{2} E. \quad (23)$$

Figure 4 shows the contributions $J_{s\theta}$ resulting from the RTA as well as from the full numerical calculation. The two are completely different. Most prominently, the hot-spot picture^{8,10–12} is no longer valid if forward-scattering corrections are taken into account. As discussed above, the scattering off spin fluctuations is strongest in the hot regions since the spin susceptibility is peaked at \mathbf{Q}_{e1} and \mathbf{Q}_{e2} , see Fig. 1. Thus the lifetimes are shorter and the RTA vector mean free paths given in Eqs. (12) and (13) are smaller. This is indeed reflected by the suppressed current contributions in the hot regions shown in Figs. 4(a) and 4(b). However, no signatures of hot regions are seen in the full results in Figs. 4(c) and 4(d). This is due to the anisotropy of the scattering rate. In the hot regions, the anisotropy $a_{s\theta}'$ is enhanced relative to the cold regions and, according to Eqs. (19)–(21), this leads to an enhancement of the vector mean free path, as was discussed in section IV. Thus the reduction of the lifetimes is compensated by the enhanced scattering anisotropy and the contribution of the hot regions to the current is comparable to that of other parts of the Fermi

pockets, i.e., the short-circuiting of the hot spots does not occur. This insight is a central result of our work.

Figure 4 also shows that the holes contribute negatively to the total current in the full calculation. In the semiclassical picture, this means that the holes drift in the same direction as the electrons. The insights gained in section IV illuminate this behavior: For the set of parameters chosen in Fig. 4, the scattering anisotropy averaged over all Fermi states is close to unity, $\langle a \rangle_\theta = 0.96$. As discussed in section IV, such a huge anisotropy leads to an effective relaxation time that is much longer than the lifetime. In effect, during the relaxation, an electron initially on the hole Fermi pocket scatters multiple times between states on the hole pocket and states on the electron Fermi pockets, which have nearly opposite velocity. Since there are more states on the electron pockets than on the hole pocket, the electron spends the larger part of the time on the electron pockets. The electron thus on average drifts in the opposite direction to what one would get if it stayed on the hole pocket. The RTA is not sensitive to the inversion of the velocity upon inter-pocket scattering and thus cannot account for this effect.

C. Transport coefficients

The transport coefficients can be obtained from the vector mean free paths. The conductivity tensor is given in Eq. (14), while the thermoelectric tensor reads²⁷

$$\alpha^{ij} = -\frac{\pi^2 k_B^2 T}{3e} \frac{\partial \sigma^{ij}}{\partial \mu}. \quad (24)$$

We will focus on the resistivity

$$\rho = \frac{1}{\sigma^{xx}}, \quad (25)$$

the Hall coefficient,

$$R_H = \frac{\sigma^{xy}}{(\sigma^{xx})^2 B}, \quad (26)$$

the Seebeck coefficient (thermopower),

$$S = -\frac{\alpha^{xx}}{\sigma^{xx}}, \quad (27)$$

and the Nernst coefficient,

$$\mathcal{N} = \frac{\sigma^{xy} \alpha^{xx} - \sigma^{xx} \alpha^{xy}}{(\sigma^{xx})^2 B}. \quad (28)$$

We give the resistivity in units of

$$\rho_0 \equiv \frac{\hbar}{e^2} \frac{\hbar W_{\text{sf}}}{\mathcal{V}_0} \times 10^{-2} (\text{eV})^2, \quad (29)$$

where \mathcal{V}_0 is the volume of the unit cell, and the Nernst coefficient in units of

$$\mathcal{N}_0 \equiv \frac{\mathcal{V}_0}{e \rho_0} \times 10^{-5} \text{ V/K}. \quad (30)$$

For the scattering strength ratio we choose in the following $W_{\text{imp}}/W_{\text{sf}} = 10^{-3}$.

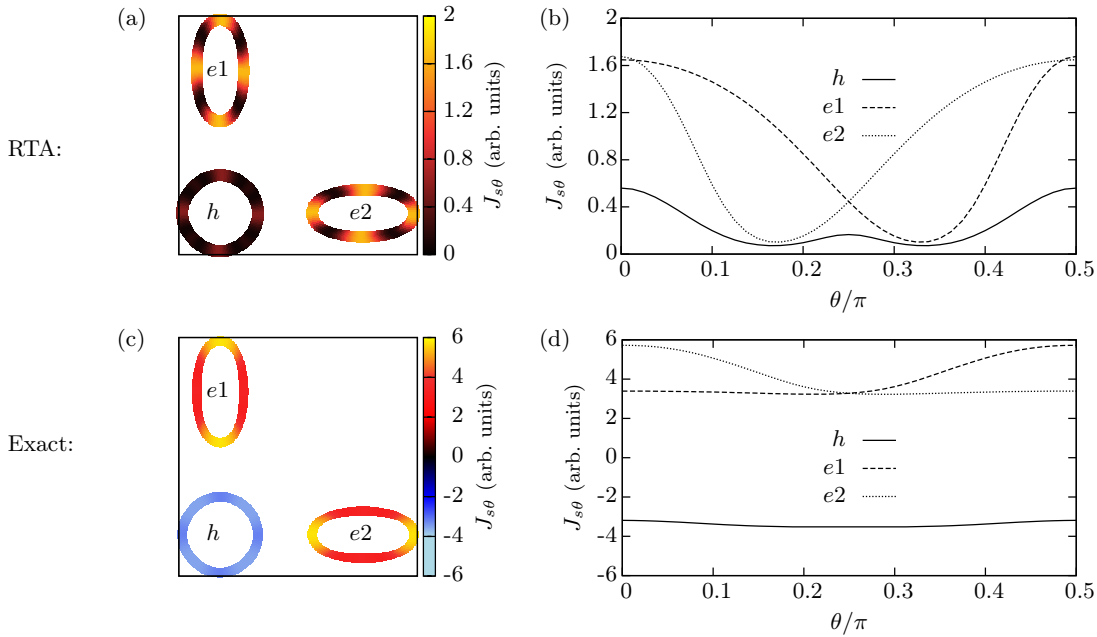


Figure 4. (Color online) Contributions to the current of states on the Fermi surface. Panels (a) and (b) show the RTA result as a color map and as a line plot along a quarter of the Fermi pockets, respectively. Note the reduction of the current contributions in the hot regions. Panels (c) and (d) show the same for the full numerical results. The large anisotropy leads to negative current contributions from the hole pocket. No signatures of hot spots are apparent. The parameters are $\xi = 2.5$, $n = 2.08$, $T = 1$ K, and $W_{\text{imp}}/W_{\text{sf}} = 0$.

1. Comparison of approximations

Figure 5 shows the temperature dependence of the transport coefficients, comparing the full numerical result with the RTA and the AA. We see that the RTA results tend to coincide with the full calculation only at very high and very low temperatures, where the scattering is nearly isotropic, see Fig. 3. In the temperature range with strong anisotropy (20–150 K) the deviations from the RTA are huge. On the other hand, the AA shows qualitative agreement with the full results over all temperatures and for both ellipticities. The agreement is even quantitative for the resistivity. It is the worst for the Nernst coefficient \mathcal{N} but even here the positive and negative extrema in \mathcal{N} are predicted by the AA close to the correct temperatures. For $\xi = 1$ the AA is slightly better than for $\xi = 2$ since the former value leads to less eccentric electron pockets. The close agreement between the AA and the full numerical results shows that the transport behavior does not sensitively depend on the precise details of the anisotropic scattering, and thus justifies our use of the approximate susceptibility in Eq. (3).

Both the RTA and the full results show strong temperature dependence. For the RTA, this can be traced back to the nontrivial geometry of the Fermi pockets leading to the hot-spot structure for high scattering anisotropies. However, as discussed in subsection VB, forward-scattering corrections invalidate the hot-spot picture for strong anisotropies. The temperature dependence of the RTA results thus stems from the wrong

origin. The true temperature dependence can be understood on the basis of the AA, which gives qualitatively correct results. Here, it is due to the strong temperature dependence of the anisotropy parameters $a_{s\theta}^{s'}$ shown in Fig. 3(b), i.e., it relies on the *corrections* to the RTA in Eqs. (10) and (11) as well as (19)–(21).

The differences between the RTA and the full results for the resistivity and the Hall coefficient are consistent with the predictions of Ref. 15 for two circular Fermi pockets. In the resistivity, we note that the expected enhancement and reduction for high and low scattering anisotropies, respectively, lead to a more pronounced change of slope compared to the RTA. Although the difference between the RTA and the full resistivity is relatively small compared to the large corrections to the electron and hole contributions shown in Fig. 4, these corrections have opposite signs and thus partially compensate each other, as already found for circular Fermi pockets in Refs. 14 and 15. The predicted enhancement of the Hall coefficient is also present.^{14,15} However, the extremum of the Hall coefficient in Fig. 5 is due to the maximum in the scattering anisotropy (cf. Fig. 3) and is thus of different origin than in Ref. 15, where a maximum in the Hall coefficient was predicted for the case that the anisotropy crosses a characteristic anisotropy level at which the mobilities of holes and electrons are of equal magnitude but opposite sign. We do not see any signatures of such a crossing in the present results. For the thermoelectric effects, Fig. 5 shows that the RTA results are even qualitatively incorrect, with the Seebeck

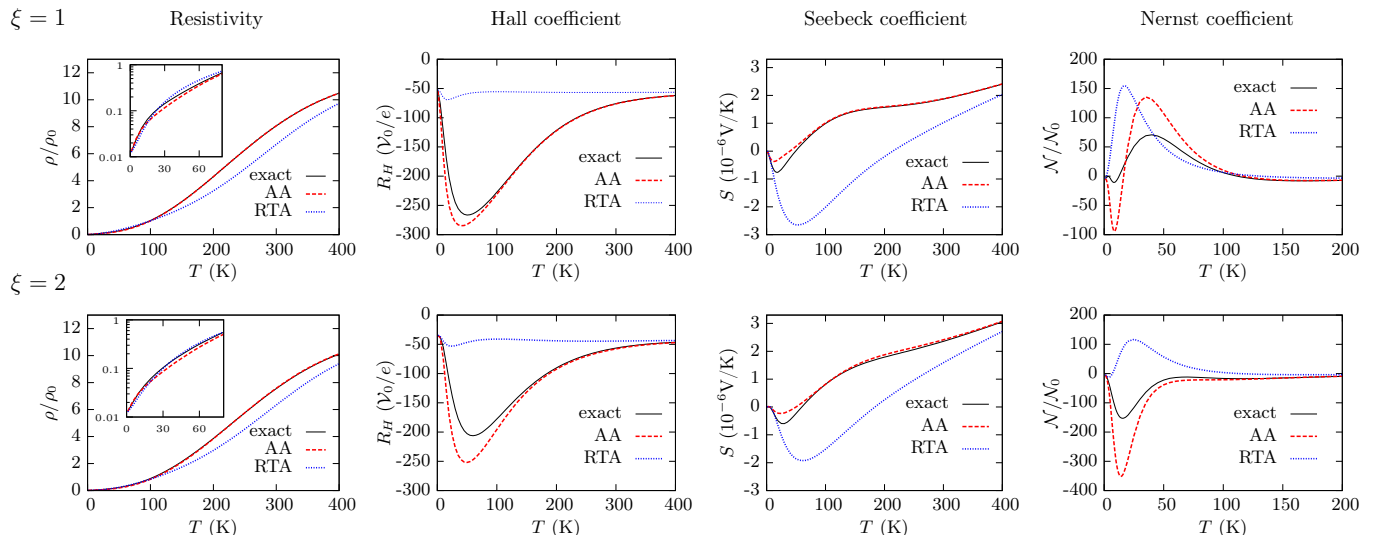


Figure 5. (Color online) Temperature dependence of transport coefficients for filling $n = 2.05$ and ellipticity parameters $\xi = 1$ and $\xi = 2$, calculated with three different methods: Numerically (“exact”), semianalytically within the anisotropy approximation (“AA”) of Eqs. (19)–(21), and within the RTA, Eqs. (12) and (13).

and Nernst coefficients showing the wrong sign in the temperature range with strong scattering anisotropy. According to Eqs. (24) and (27), the Seebeck coefficient S is proportional to $\partial \ln \sigma^{xx} / \partial \mu = -\partial \ln \rho / \partial \mu$. In the RTA, it stems from the shift of the hot spots with the chemical potential, i.e., with doping. In the full results and the AA, it is instead due to the change in the anisotropy parameters $\alpha_{s\theta}'$ with the chemical potential. Figure 5 shows that for the chosen parameters, the two effects contribute to S with opposite sign. The full results for the Nernst coefficient \mathcal{N} change sign between the ellipticities $\xi = 1$ and $\xi = 2$. This effect is missed by the RTA. We return to the Nernst coefficient below.

Qualitative differences between the RTA and the full solution of the Boltzmann equation have also been reported for single-band cuprate models with strongly anisotropic scattering.^{18,27} The physics discussed here, including the inverted vector mean free path of minority carriers, rely on the presence of multiple bands and Fermi pockets, though.

2. Doping dependence

We now turn to the doping dependence of the transport coefficients. Figures 6(a)–6(d) show the full solutions at different fillings, while Fig. 6(e) shows the current contributions of states on the Fermi surfaces at the two temperatures $T = 100$ K and $T = 400$ K with strong and weak scattering anisotropy, respectively. Note that the current contributions from the hole pocket are negative for $T = 100$ K and $n \gtrsim 1.99$, i.e., towards the electron-doped side. On the hole-doped side, the scattering is more isotropic due to the large discrepancy in size between the electron and hole pockets.

At high temperatures, the transport coefficients all show a smooth doping dependence resulting from the change in the Fermi surfaces and velocities in the presence of mostly isotropic scattering. In the intermediate temperature range, where anisotropic scattering is strong, this is overlaid by nontrivial doping dependence due to the forward-scattering corrections.

The resistivity around $T \approx 100$ K is largest for intermediate fillings, for which the Fermi pockets are well nested. This is because the narrow peaks in the spin susceptibilities at \mathbf{Q}_{e1} and \mathbf{Q}_{e2} lead to efficient scattering only for nested Fermi pockets. The inefficiency of anisotropic scattering for small and large n causes a rapid decrease in the resistivity with doping, as shown in the inset in Fig. 6(a). Note that the *relative* change in ρ with doping is much larger here than at high temperatures. Since the Seebeck coefficient S is proportional to $\partial \ln \sigma^{xx} / \partial \mu = -\partial \ln \rho / \partial \mu = -\rho^{-1} \partial \rho / \partial \mu$, it is sensitive to this relative change in ρ with μ or n and is, therefore, strongly enhanced in the intermediate temperature range with strong scattering anisotropy, as Fig. 6(c) clearly shows.

For the Hall coefficient R_H , Fig. 6(b), one would naively expect the largest and smallest values for the most strongly hole-doped and electron-doped cases, respectively, since electrons and holes contribute with opposite signs. This is indeed the case at $T \approx 400$ K, where the scattering is nearly isotropic and no negative current contributions occur. At $T \approx 100$ K, however, Fig. 6(b) shows a strong negative enhancement of R_H for intermediate filling. According to Fig. 6(e), the contribution of the holes to the total current is negative in this range. In the semiclassical picture this means that the holes drift in the same direction as the electrons, reducing the charge current. Irrespective of that, the magnetic field deflects

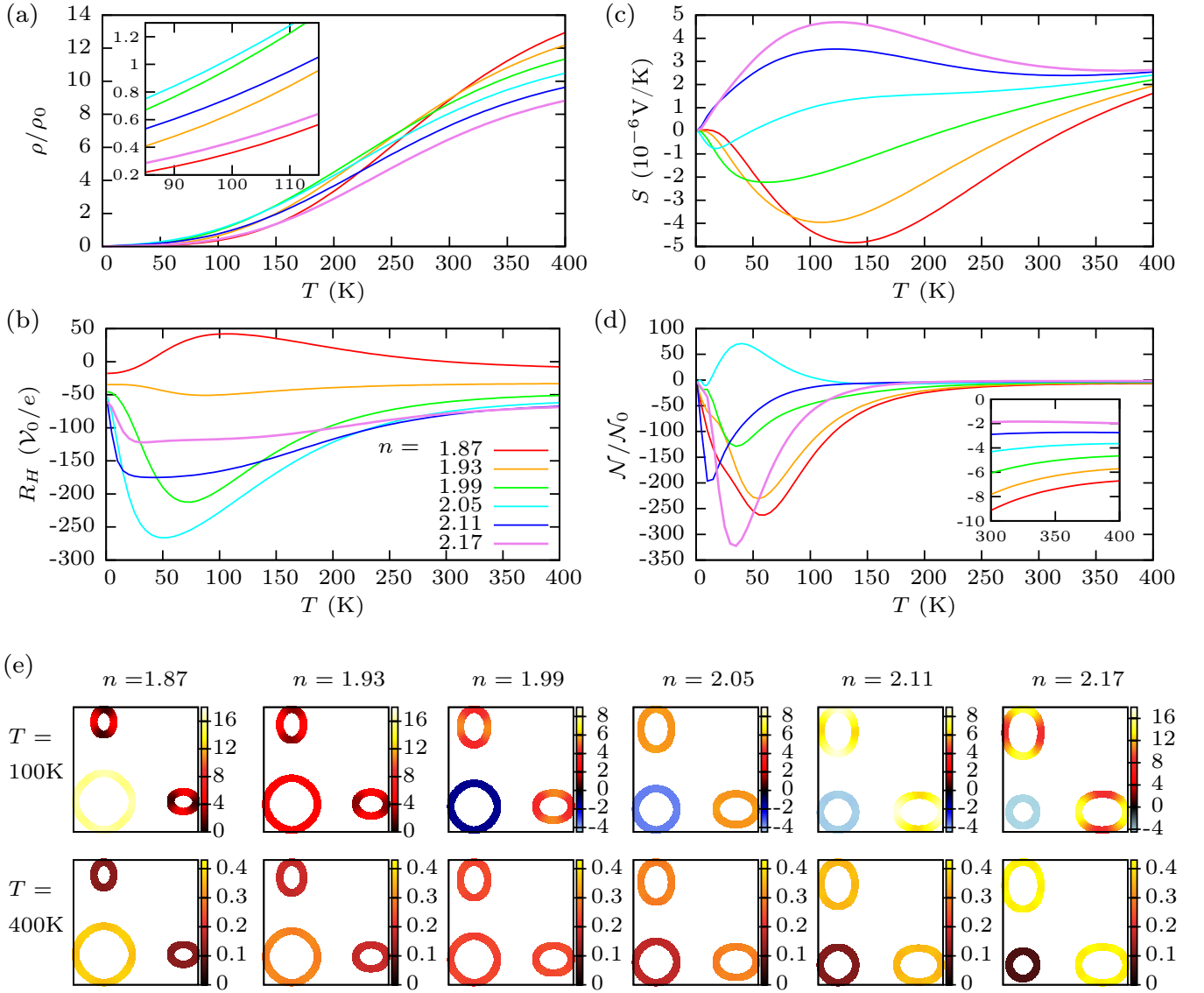


Figure 6. (Color online) (a) Resistivity, (b) Hall coefficient, (c) Seebeck coefficient, and (d) Nernst coefficient as functions of temperature for different fillings n . (e) State-resolved current contributions for $T = 100$ K and $T = 400$ K for all fillings considered. Note the different color scales.

the holes and the electrons in the same direction. Hence, the inverted sign of the hole contribution reduces the charge current without changing the Hall voltage. This gives rise to an enhancement of the Hall coefficient defined as the Hall voltage relative to the charge current.

The Nernst coefficient \mathcal{N} plotted in Fig. 6(d) is highly sensitive to small doping changes and also, as is evident from Fig. 5, to changes in the band parameters. Equations (24)–(26) and (28) show that

$$\mathcal{N} = \frac{3e}{\pi^2 k_B^2 T} \frac{\partial}{\partial \mu} \frac{R_H}{\rho} = \frac{3e}{\pi^2 k_B^2 T} \frac{\partial n}{\partial \mu} \frac{\partial}{\partial n} \frac{R_H}{\rho}. \quad (31)$$

The Nernst coefficient is thus sensitive to the nonmonotonic doping dependence of both ρ and R_H . For the cases we have considered, the contributions from ρ and R_H

usually counteract each other. The complicated behavior of \mathcal{N} , for example the different sign of \mathcal{N} for $n = 2.05$ compared to the other fillings, is thus due to the quantitative competition of the doping dependences of ρ and R_H and not to any clear qualitative features in the Fermi surfaces or the scattering. This suggests that the other coefficients might be more advantageous as probes of the electronic system. However, the detailed comparison of experimental transport coefficients and calculations for realistic models remains work for the future.

VI. CONCLUSIONS

We have studied transport in a two-band model relevant for the iron pnictides, using the semiclassical Boltzmann equation. Forward-scattering corrections due to anisotropic interband scattering off spin fluctuations have been included. Spin fluctuations have been described by a phenomenological Millis-Monien-Pines susceptibility,²¹ with temperature-dependent parameters chosen based on neutron-scattering results for the pnictides.²² Our analytical and numerical investigations show that the anisotropic scattering gives rise to unusual transport behavior. Most surprisingly, the hot spots are *not* short-circuited by the cold regions of the Fermi pockets even for very strong scattering. The enhanced scattering rate in the hot regions indeed leads to a short lifetime there, but this effect is balanced by the enhanced vector mean free path due to the anisotropic scattering. This breakdown of the concept of hot and cold regions is not found in a simple RTA neglecting forward-scattering corrections.

The nearly isotropic contribution of states around the Fermi pocket to the transport, even for strongly elliptical electron pockets, justifies the discussion of transport in terms of isotropic mobilities for each pocket. However, as discussed for the case of circular pockets,^{14,15} the mobility of the minority carriers can turn negative in the regime of highly anisotropic scattering. In the present work, negative mobility corresponds to inverted vector mean free paths and the resulting negative current contributions.

The contribution of hot spots to the transport and the occurrence of negative currents are the main features that distinguish the transport properties of pnictides from previously considered one-band systems with similarly anisotropic scattering. In this work, we have presented unusual temperature and doping dependences of various transport coefficients. Beyond this, negative current contributions can also lead to a negative magnetoresistance.¹⁵ However, the present model with two electron pockets and one hole pocket does not show negative magnetoresistance in the considered parameter range. Calculations of transport coefficients for more realistic pnictide models are desirable to allow quantitative predictions.

ACKNOWLEDGMENTS

Financial support by the Deutsche Forschungsgemeinschaft through Research Training Group GRK 1621 is gratefully acknowledged. The authors thank J. Schmiedt, H. Kontani, and O. Kashuba for useful discussions.

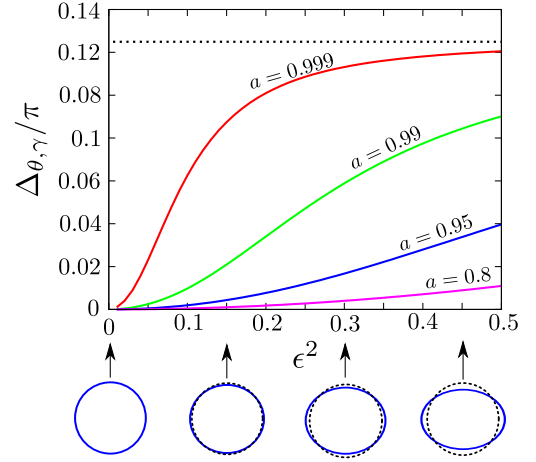


Figure 7. (Color online) Effective angular shift $\Delta_{\theta,\gamma}$ for the state $\theta = \pi/8$ as a function of ϵ^2 for different uniform anisotropies a . ϵ represents the eccentricity of the electron pocket. The shift is directed towards the hot spot at $\theta = \pi/4$, hence the maximal value of $\Delta_{\theta,\gamma}/\pi$ is $1/8$. The insets indicate the shape of the electron pocket (solid line) corresponding to various values of ϵ^2 .

APPENDIX: DISCUSSION OF THE ANGULAR SHIFT

As discussed in the main text, the vector mean free path of a state $|s, \theta\rangle$ can be written as a power series in the anisotropy parameter, where the term of order n contains the RTA vector mean free path of a state reached by n hopping events towards the closest hot spot. We have argued that the angular shift towards the hot spot is a small effect for the vector mean free path for realistic ellipticities of the electron pockets and have therefore ignored it above. We here explore this effect analytically within a simple model. To get an estimate for the upper limit of the correction to the vector mean free path, it is sufficient to consider only a *single* electron pocket. Our simple model consists of a circular hole Fermi pocket with the Fermi wave number k and an elliptical electron Fermi pocket described by the semi-major and semi-minor axis $k_a = k(1 - \epsilon^2)^{-1/4}$ and $k_b = k(1 - \epsilon^2)^{1/4}$, respectively, where ϵ is the eccentricity of the ellipse. To focus on the shift effect we assume constant anisotropy, $a_{s\theta}' = a$. For two Fermi pockets and constant anisotropy, Eq. (17) takes the form

$$\Lambda_{s\theta} = \Lambda_{s\theta}^{(0)} + a \Lambda_{s\bar{\theta}}, \quad (32)$$

where $\bar{h} = e$, $\bar{e} = h$, and the RTA solution $\Lambda^{(0)}$ is given by Eq. (12). Using simple trigonometry, we find that for the given geometry, the difference between $\bar{\theta}$ and θ to leading order in the eccentricity ϵ reads $\frac{\epsilon^4}{16} \sin 4\theta$. Iterating Eq. (32), we obtain the solution for the electron pocket as

$$\Lambda_{e\theta} = \sum_{n=0}^{\infty} a^{2n} (\Lambda_{e\theta_n}^{(0)} + a \Lambda_{h\theta_n}^{(0)}), \quad (33)$$

with

$$\theta_n = \theta_{n-1} + \frac{\epsilon^4}{16} \sin 4\theta_{n-1} \quad \text{and} \quad \theta_0 = \theta. \quad (34)$$

The solution for the hole pocket follows immediately from Eqs. (32) and (33).

Replacing the discrete index n by a continuous variable, we obtain

$$\Lambda_{e\theta} = -\frac{2 \ln a}{1-a^2} \int_0^\infty dn a^{2n} (\Lambda_{e\theta_n}^{(0)} + a\Lambda_{h\theta_n}^{(0)}) + \mathbf{R}, \quad (35)$$

with a correction \mathbf{R} . By splitting the integration range into intervals $[m, m+1]$ with integer m , one can easily show that

$$|\mathbf{R}| \leq \sum_n a^{2n} \left| (\Lambda_{e\theta_n}^{(0)} + a\Lambda_{h\theta_n}^{(0)}) - (\Lambda_{e\theta_{n+1}}^{(0)} + a\Lambda_{h\theta_{n+1}}^{(0)}) \right|, \quad (36)$$

which is obviously of higher order in ϵ^2 because of Eq. (34). Substituting $n = 4 \ln(1+z)/\epsilon^4$ we obtain

$$\Lambda_{e\theta} = \frac{1}{1-a^2} \int_0^\infty dz \gamma \left(\frac{1}{1+z} \right)^{\gamma+1} (\Lambda_{e\theta(z)}^{(0)} + a\Lambda_{h\theta(z)}^{(0)}), \quad (37)$$

with

$$\gamma \equiv 8 \frac{\ln(1/a)}{\epsilon^4} \quad (38)$$

and

$$\theta(z) \equiv \frac{1}{2} \arctan [(z+1) \tan 2\theta]. \quad (39)$$

In the integral in Eq. (37), the factor $\gamma [1/(1+z)]^{\gamma+1}$ acts as a distribution function which is normalized to unity and becomes a δ -function in the limit of zero ellipticity, i.e., for $\gamma \rightarrow \infty$. Hence, the largest shifts are

achieved for small values of γ , which, according to Eq. (38), correspond to large scattering anisotropy and large ellipticity.

The shift also depends on the position on the Fermi pocket. There is no shift at the hot spots, $\theta = (2n-1)\pi/4$, and at the cold spots, $\theta = n\pi/2$. The largest shift can be expected to occur between the hot and cold spots, in the vicinity of $(2n-1)\pi/8$.

We can make further analytical progress by expanding the vector $(\Lambda_{e\theta(z)}^{(0)} + a\Lambda_{h\theta(z)}^{(0)})$ to linear order in $\theta(z)$. This is best justified if the total angular shift is small, i.e., if we start with θ close to a hot spot. However, the total shift can never be larger than $\pi/4$ so that the approximation always gives at least qualitatively correct results for not excessive eccentricities. Equation (37) can then be written as

$$\Lambda_{e\theta} = \frac{1}{1-a^2} (\Lambda_{e,\theta+\Delta_{\theta,\gamma}}^{(0)} + a\Lambda_{h,\theta+\Delta_{\theta,\gamma}}^{(0)}), \quad (40)$$

with the effective angular shift

$$\begin{aligned} \Delta_{\theta,\gamma} &= \int_0^\infty dz \gamma \left(\frac{1}{1+z} \right)^{\gamma+1} \theta(z) - \theta \\ &\cong \frac{\sin 4\theta}{32} \frac{\epsilon^4}{\ln(1/a)} + \frac{\sin 8\theta}{512} \left[\frac{\epsilon^4}{\ln(1/a)} \right]^2 \\ &\quad + \mathcal{O} \left(\left[\frac{\epsilon^4}{\ln(1/a)} \right]^3 \right). \end{aligned} \quad (41)$$

By neglecting the shift, $\Delta_{\theta,\gamma} = 0$, we would obtain the analogue of Eqs. (19)–(21) for the case of constant anisotropy and a single electron pocket.

In Fig. 7 we plot the angular shift at $\theta = \pi/8$ for different anisotropies as a function of the eccentricity squared, ϵ^2 . Realistic scattering anisotropies hardly exceed the value $a = 0.95$, for which the shift is small up to $\epsilon^2 \approx 0.5$. Stronger ellipticities might, however, lead to significant corrections.

* maxim.breitkreiz@tu-dresden.de

† carsten.timm@tu-dresden.de

¹ D. C. Johnston, Adv. Phys. **59**, 803 (2010).

² L. Taillefer, Annu. Rev. Condens. Matter Phys. **1**, 51 (2010).

³ Z. W. Zhu, Z. A. Xu, X. Lin, G. H. Cao, C. M. Feng, G. F. Chen, Z. Li, J. L. Luo, and N. L. Wang, New J. Phys. **10**, 063021 (2008); Q. Tao, Z. W. Zhu, X. Lin, G. H. Cao, Z. A. Xu, G. F. Chen, J. L. Luo, and N. L. Wang, J. Phys.: Condens. Matter **22**, 072201 (2010).

⁴ E. D. Mun, S. L. Bud'ko, N. Ni, A. N. Thaler, and P. C. Canfield, Phys. Rev. B **80**, 054517 (2009); H. Hodovanets, A. Thaler, E. Mun, N. Ni, S. L. Bud'ko, and P. C. Canfield, Philos. Mag. **93**, 661 (2013).

⁵ A. Kondrat, J. E. Hamann-Borrero, N. Leps, M. Kosmala, O. Schumann, A. Köhler, J. Werner, G. Behr, M. Braden, R. Klingeler, B. Büchner, and C. Hess, Eur. Phys. J. B **70**, 461 (2009); C. Hess, A. Kondrat, A. Narduzzo, J. E.

Hamann-Borrero, R. Klingeler, J. Werner, G. Behr, and B. Büchner, Europhys. Lett. **87**, 17005 (2009); A. Kondrat, G. Behr, B. Büchner, and C. Hess, Phys. Rev. B **83**, 092507 (2011).

⁶ P. Prelovšek, I. Sega, and T. Tohyama, Phys. Rev. B **80**, 014517 (2009); P. Prelovšek and I. Sega, *ibid.* **81**, 115121 (2010).

⁷ M. Matusiak, Z. Bukowski, and J. Karpinski, Phys. Rev. B **81**, 020510 (2010).

⁸ M. J. Eom, S. W. Na, C. Hoch, R. K. Kremer, and J. S. Kim, Phys. Rev. B **85**, 024536 (2012).

⁹ K. Ohgushi and Y. Kiuchi, Phys. Rev. B **85**, 064522 (2012).

¹⁰ S. Arsenijević, H. Hodovanets, R. Gaál, L. Forró, S. L. Bud'ko, and P. C. Canfield, Phys. Rev. B **87**, 224508 (2013).

¹¹ E. C. Blomberg, M. A. Tanatar, R. M. Fernandes, I. I. Mazin, B. Shen, H.-H. Wen, M. D. Johannes, J. Schmalian, and R. Prozorov, Nature Commun. **4**, 1914 (2013).

- ¹² R. M. Fernandes, E. Abrahams, and J. Schmalian, Phys. Rev. Lett. **107**, 217002 (2011).
- ¹³ A. F. Kemper, M. M. Korshunov, T. P. Devereaux, J. N. Fry, H.-P. Cheng, and P. J. Hirschfeld, Phys. Rev. B **83**, 184516 (2011).
- ¹⁴ L. Fanfarillo, E. Cappelluti, C. Castellani, and L. Benfatto, Phys. Rev. Lett. **109**, 096402 (2012).
- ¹⁵ M. Breitzkreiz, P. M. R. Brydon, and C. Timm, Phys. Rev. B **88**, 085103 (2013).
- ¹⁶ R. Hlubina and T. M. Rice, Phys. Rev. B **51**, 9253 (1995).
- ¹⁷ A. Rosch, Phys. Rev. Lett. **82**, 4280 (1999).
- ¹⁸ H. Kontani, Rep. Prog. Phys. **71**, 026501 (2008).
- ¹⁹ P. M. R. Brydon, J. Schmiedt, and C. Timm, Phys. Rev. B **84**, 214510 (2011).
- ²⁰ I. Eremin and A. V. Chubukov, Phys. Rev. B **81**, 024511 (2010).
- ²¹ A. J. Millis, H. Monien, and D. Pines, Phys. Rev. B **42**, 167 (1990).
- ²² D. S. Inosov, J. T. Park, P. Bourges, D. L. Sun, Y. Sidis, A. Schneidewind, K. Hradil, D. Haug, C. T. Lin, B. Keimer, and V. Hinkov, Nature Phys. **6**, 178 (2010).
- ²³ S. O. Diallo, D. K. Pratt, R. M. Fernandes, W. Tian, J. L. Zarestky, M. Lumsden, T. G. Perring, C. L. Broholm, N. Ni, S. L. Bud'ko, P. C. Canfield, H.-F. Li, D. Vaknin, A. Kreyssig, A. I. Goldman, and R. J. McQueeney, Phys. Rev. B **81**, 214407 (2010).
- ²⁴ M. J. Rice, Phys. Rev. **159**, 153 (1967).
- ²⁵ E. H. Sondheimer, Proc. R. Soc. London, Ser. A **268**, 100 (1962).
- ²⁶ P. L. Taylor, Proc. R. Soc. London, Ser. A **275**, 200 (1963).
- ²⁷ D. I. Pikulin, C.-Y. Hou, and C. W. J. Beenakker, Phys. Rev. B **84**, 035133 (2011).